EXCITED STATES AND VIBRATIONAL SPECTROSCOPY OF ICE AND ADSORBED BIOMOLECULES

A Thesis
Presented to
The Academic Faculty

by

Vernon D. Crowell Jr.

In Partial Fulfillment
of the Requirements for the Degree
Master of Science in the
School of Chemistry

Georgia Institute of Technology
December 2014
Copyright 2014 by Vernon D Crowell Jr

EXCITED STATES AND VIBRATIONAL SPECTROSCOPY OF ICE AND ADSORBED BIOMOLECULES

Approved by:

Dr. David Sherrill, Advisor
School of Chemistry and Biochemistry
Georgia Institute of Technology

Dr. Thomas Orlando
School of Chemistry and Biochemistry
Georgia Institute of Technology

Dr. Jean-Luc Bredas
King Abdullah University of Science and Technology

Date Approved: 8/20/2014

ACKNOWLEDGEMENTS

I would like to thank Dr. David Sherrill and Dr. Thomas Orlando for being outstanding advisors and making this thesis possible. I thank the friends I have made in the chemistry department for their moral support these past few years. I also thank Rob Parrish, Trent Parker, Michael Marshall, and others in the lab for many great times. I would specifically like to thank Dr. Alice DeSimone, who is responsible for all of the experimental work in the chapter on water ice. I also thank Dr. Anton Sidorov for many helpful discussions. Finally, I would like to thank the funding sources of the projects I worked on: a Presidential Fellowship from Georgia Tech, the National Science Foundation (Grant No. CHE-1011360), and the NASA Outer Planets Program under contract NNX10AB03G.

TABLE OF CONTENTS

LIST OF FIGURES

SUMMARY

The following thesis focuses mainly on the challenging problem of the dynamics of excited water ice. Work was done in conjunction with experimentalists in order to elucidate a possible desorption mechanism for water molecules on an ice surface. Electronic structure computations have been used to probe the excited states of water ice and the mechanisms of desorption. The third chapter involves work on computing the Raman spectra of DNA nucleobases on a graphene surface.

CHAPTER 1

INTRODUCTION

The work presented in this thesis exhibits how modern electronic structure theory can be used to solve complex problems. The majority of the work focuses on the excited state dynamics of water ice. Use of modern electronic structure methods allowed the elucidation of a dipole reversal mechanism for desorption in ice. It has been known for a long time that exciting a gas phase water molecule to the first excited singlet state results in a dipole reversal in the water. Electron density is shifted from the oxygen to the hydrogen. This results in the dissociation of the molecule. However, in the condensed phase, coupling to neighboring water molecules leads to charge delocalization and potential pathways to desorption of intact water molecules.

The other work in the thesis involves predicting the Raman spectrum of DNA nucleobases on a graphene surface. Raman spectroscopy has recently been used by the Orlando group to monitor damage events to DNA after irradiation by low energy electrons. The work shown here was done in part to aid experiment by calculating the shift in the Raman spectra of nucleobases due to the surface effects of graphene.

CHAPTER 2

MECHANISMS OF H_2O DESORPTION FROM AMORPHOUS SOLID WATER BY 157-NM IRRADIATION: AN EXPERIMENTAL AND THEORETICAL STUDY

[Previously Published in

A.J. DeSimone, V.D. Crowell, C.D. Sherrill, T.M. Orlando. Mechanisms of H2O Desorption from Amorphous Solid Water by 157-nm Irradiation: An Experimental and Theoretical Study, Journal of Chemical Physics **139**, 164702 (2013)]

2.1. INTRODUCTION

Water ice is present on many low-temperature surfaces in the ring system of Saturn and throughout the outer solar system,[1, 2] and these icy grains are exposed to ultraviolet (UV) radiation. Even in astrophysical environments beyond the solar system, photodesorption of water by the far-UV component of the interstellar radiation field has been proposed to account for the large amount of water in the gas phase above cold surfaces.[3] Investigating the mechanisms and determining the cross section of water photodesorption from amorphous solid water (ASW) and crystalline ice (CI) are essential to understanding the electronic properties of these icy surfaces and the lifetime of ice in various solar system environments.

The first excited state of an isolated water molecule is dissociative, as it contains a hole in the $1b_1$ non-bonding orbital and an electron in the $4a_1$ anti-bonding orbital. However, in the condensed phase, coupling to neighboring water molecules leads to charge delocalization and potential pathways to desorption of intact water molecules.[4]

For ASW and CI, insulating materials in which holes and electrons have significant lifetimes before recombination, excited electronic states can be considered excitons, which may have Frenkel and Wannier character. The first excited state becomes a band of $1b_1 \rightarrow 4a_1$ transitions with ~7-9.5 eV, peaked at 8.7 eV, and the second band includes higher $1b_1 \rightarrow 4a_1$ exciton states as well as $3a_1 \rightarrow 4a_1$ transitions and peaks at ~10.2 eV.[5]

Several experimental studies of water desorption have been performed using radiation sources with energies in these two UV absorption bands, including a broadband (7–10.5 eV) hydrogen discharge lamp,[6] a more narrow Lyman-alpha source at 10.2 eV,[7, 8] two 248-nm photons at a total energy of 9.99 eV,[9] and an excimer laser at 7.89 eV.[10] The latter two experiments utilized pulsed lasers and yielded time-of-flight spectra, which were fit with Maxwell-Boltzmann distributions characterized by translational temperatures, T_{trans}. The 9.99 eV radiation yielded T_{trans} = 770 K,[9] while the 7.89 eV radiation yielded T_{trans} = 1800 K.[10] The authors of these two studies also interpreted the results in terms of two different mechanisms. Hama et al.[10] supported the kick-out mechanism that was modeled using molecular dynamics simulations.[11] The kick-out mechanism involves the transfer of momentum to a nearby H_2O molecule by a hot H atom produced by photodissociation. Nishi et al.[9] previously proposed a more direct mechanism that involved the exchange repulsion between an excited water molecule and the surface. This exchange repulsion energy could lead to exciton migration, self-trapping at a surface, and eventual desorption of water molecules. In this case, though not stated in the model, the excitation can be visualized as a dipole reversal, and the resulting forces act to repel the excited water molecule from the surface. Another mechanism that may

contribute to water desorption is recombination of photoproducts, in which the desorption signal increases with temperature.[12]

Previous theoretical work has shown that exciton delocalization competes with dissociation of water in ice. The GW approximation (the expansion of self-energy in terms of the Green's function, G, and the screened Coulomb interaction, W) using Kohn-Sham eigenvalues and the Bethe-Salpeter equation revealed exciton diffusion in hexagonal ice.[13] Quantum-dynamical simulations performed on a variety of hexamer isomers showed that delocalization of the exciton is on the same femtosecond time scale as photodissociation.[14] Even though the first excited state of an isolated water molecule is dissociative, condensed-phase water molecules may remain intact when excited due to intermolecular interactions. Previous theoretical studies on the nature of the excited state and delocalization probabilities have not investigated the possible role of dipole reversal in the competition between photodesorption and photodissociation of water molecules.

The aims of the present study are to discover the nature of the excited states that are involved in H_2O photodesorption, to examine mechanisms other than kick out by a hot H atom, and to determine the cross section for water removal from ASW at 7.9 eV. The photodesorption of H_2O from ASW due to 157-nm radiation has been studied using resonance-enhanced multiphoton ionization (REMPI). The experimental approach is ostensibly the same as that used previously by Hama et al.[10] Rotational and translational energies of the desorbed water molecules have been determined by comparison with simulations. H^+ and OH^+ fragment ions have been detected with non-resonant multiphoton ionization, and the translational energies of their vibrationally excited parent water molecules have been deduced. The cross section for ice removal by 7.9-eV photons

has been measured for various thicknesses, and the possible role of dipole reversal in desorption has been examined using *Ab Initio* Molecular Dynamics (AIMD) simulations. Though similar experimental measurements have been reported,[10] absolute cross section values have not been determined at 7.9 eV, and the nature of the electronically excited surface states of ice have not been examined directly. Section 2 describes the experiment, data analysis procedures, and theoretical methods. The experimental and theoretical results are presented in Sections 3 and 4, respectively. The photodesorption mechanism, cross sections, and astrophysical relevance are discussed in Section 5 with conclusions given in Section 6.

2.2 EXPERIMENTS AND DATA ANALYSIS

2.2.1 Laboratory Measurements

Photodesorption experiments were performed in an ultra-high vacuum (UHV) chamber that has been previously described in detail.[15] Briefly, the UHV system (base pressure of 5×10^{-10} Torr) was equipped with a time-of-flight (TOF) mass spectrometer, a leak valve for dosing, and a liquid-nitrogen-cooled copper sample holder. All experiments were performed at the minimum sample temperature, 108 K, unless otherwise stated.

Unfocused 157-nm light from an excimer laser (GAM Laser, EX5) entered the chamber through a magnesium fluoride window and struck the sample at a 45° angle. To ensure that the desorption process was a single-photon event, low (typically 50-90 μJ cm^{-2} per pulse) desorption pulse energies were used. An iris was placed in the N_2-purged beam path to control the radius of the irradiated region.

Desorbed water molecules were detected with 2+1 REMPI via the C(000)-X(000) transition, which corresponds to 247.8-248.6 nm. The wavelengths were obtained by frequency doubling the visible output of a Nd:YAG-pumped optical parametric oscillator (Spectra-Physics, MOPO-SL). The beam was focused between 1 and 4 mm above the surface with a focal volume of ~10μm^3. This distance between the surface and the detection region was varied to ensure that the translational temperature obtained by fitting the data was the same at each distance.

The time between desorption and ionization was varied with a delay generator from 0 to 10 μs to probe different parts of the desorption plume. This delay time equals the flight time of the molecule from the surface to the REMPI detection region. The water peak in each mass spectrum was integrated to obtain the total water signal for each time delay. The resulting graph of water signal versus time is referred to as the TOF spectrum.

For most experiments (if coverage is not specified), background dosing was performed for 20 minutes at a water pressure of 5 x 10^{-7} Torr, resulting in 600 L exposure (1 L = 1 x 10^{-6} Torr·s). The penetration depth of a 157-nm photon through ice is 120 nm,[5] or 230 ML at 45° to normal.[16] Assuming a sticking probability of at least 0.4, the ice was thick enough that the incoming photons did not reach the underlying substrate. Doses between 50 and 1000 L were found to produce the same TOF spectra. For doses between 5 and 50 L, while the shape of the distribution remained consistent, the amount of photodesorbed water decreased with increasing exposure, presumably due to decreasing surface area as the ice surface became smoother.

Water peak areas were collected over ~100,000 pulses in order to determine cross sections for water removal, σ. Water signal was plotted versus number of incident 157-

nm photons, and the data were fit with exponential functions of the form $y = Ae^{-\sigma x}$, where x has units of photons cm^{-2}. The number of 157-nm photons was calculated using the pulse counter on the excimer laser display, the average excimer power measured before and after the scan, and a correction factor of 0.65 for losses passing through the MgF_2 window. Average excimer power was found to remain constant on the time scale of these experiments. However, the turbulent quality of the nitrogen purge in the purge tube affected the power, and much of the variation in water signal was likely due to the erratic desorption laser power. The ionization laser power was recorded at several times during these cross section measurements, and signal was corrected for the observed changes in average power.

An attempt was made to observe vibrationally excited water molecules by REMPI at 251.8-253.8 nm, where the H_2O(C-X) $\Delta v_2 = -1$ transitions occur.[17] OH^+ and H^+ signals were much stronger than H_2O^+ signals in this wavelength range, in part due to predissociation of the C(010) state. This intermediate state is known to dissociate to form neutral OH and H fragments, and these neutral fragments can be ionized via non-resonant ionization using the same laser pulse. However, this process requires at least four photons with no resonant steps. Although the lack of significant water signal between 251.8 and 253.8 nm can be explained by predissociation, the strong OH^+ and H^+ signals may also be due to single-photon-induced dissociation of vibrationally excited H_2O^+. This parent ion can be produced by 2+1 REMPI of the ground state or by single-photon ionization of an electronic excited state. Equations (1) and (2) show how an excited water molecule can become ionized and then dissociated by the absorption of subsequent photons.[17]

H_2O (C, v*) + $h\nu$ → H_2O^+ (X, v*)

(1)

H_2O^+ (X, v*) + $h\nu$ → H^+ + OH

→ H + OH^+

(2)

Because the molecule does not fragment until absorbing additional photons in the detection region, TOF measurements of the fragment ions actually probe the velocities of the parent molecules. Any additional energy imparted to H^+ or OH^+ by the fragmentation process is negligible compared to the energy gained during acceleration into the flight tube. TOF spectra for H^+ and OH^+ were obtained at 253.0 nm with a distance of 3 ± 0.5 mm between the surface and the detection region. Since these fragment ions arise from H_2O (v*) molecules, these measurements allow the H_2O (v*) velocity distribution to be determined.

2.2.2. Simulation of TOF Spectra

Simulation of TOF spectra was accomplished using the flux-weighted Maxwell-Boltzmann distribution, which is appropriate for photodesorption of chemisorbed species.[18] A simple fit of the TOF spectrum, $S(t, T_{trans})$ was slightly narrower than the data:

$$S(t, T_{trans}) = At^{-4}\exp\left(\frac{-mr^2}{2k_B T_{trans} t^2}\right),$$

(3)

where T_{trans} is the translational temperature, r is the distance between the surface and the detection volume, and A is a scaling factor. Following the work of Hama et al.,[19] we

integrated over the entire irradiated area ($0 \leq R \leq R_{max}$), where R_{max} is the radius of the desorption laser spot, the spot is approximated as a circle, and $2\pi R\, dR$ is the infinitesimal area. Fitting curves of appropriate width were obtained by using the following equation at each desired flight time (t):

$$S(R_{max}, t, T_{trans}) = \int_0^{R_{max}} \frac{\pi r R}{t^4} \left(\frac{m}{k_B T_{trans}}\right)^2 \sqrt{r^2 + R^2}\, \exp\left(\frac{-m\left(r^2+R^2\right)}{2k_B T_{trans} t^2}\right) dR, \quad (4)$$

as shown in Figure 1a, where all fitting curves used r = 2 mm.

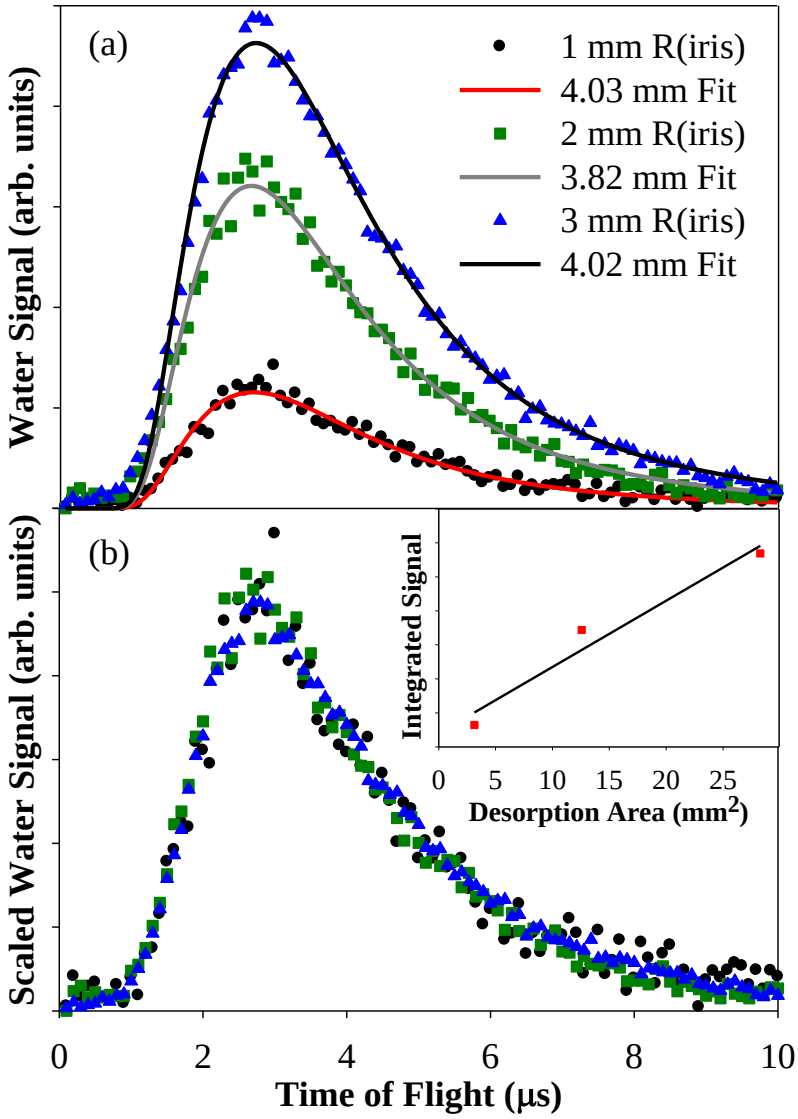

Figure 1 TOF spectra of H_2O desorbed from ASW by 157-nm photons with three different desorption laser spot sizes. The desorption laser beam passed through an iris opening with a radius of 1 mm (black circles), 2 mm (green squares), and 3 mm (blue triangles). The fits in (a) were calculated using Equation (4) with r = 2 mm, T_{trans} = 625 ± 5 K, and R_{max} ~ 4 mm (exact values in legend). In (b), the TOF spectra were scaled and overlaid to emphasize their indistinguishable shapes. The inset shows a nearly linear relationship between integrated water signal (from 0 to 10 μs) and desorption laser spot area.

However, this method of fitting the data was not supported by experiments with varying desorption laser spot sizes. An iris was inserted into the desorption beam path to change the radius of the irradiated area, which should correspond to R_{max} in Equation (4), and nearly identical spectra were produced with different iris opening radii, R(iris). Figure 1 a shows that TOF spectra obtained at R(iris) = 1, 2, and 3 mm were all fit best with R_{max} ~ 4 mm in Equation (4). Figure 1b displays those three TOF spectra scaled to the same amplitude so that their similarities can be better appreciated. Clearly, changing R(iris) from 3 mm to 1 mm did not alter the width of the TOF spectrum, as it should have according to Equation (4). In fact, the only difference between these spectra was multiplication by a scaling factor that increased nearly linearly with increasing irradiation area (inset of Figure 1b).

Although decreasing the spot size was predicted to narrow the TOF spectrum, experiments did not reveal any change in width, possibly because the ionization volume was very small ($10\mu m^3$) compared to the desorption areas tested. However, increasing the spot size significantly increased the number of detected water molecules, so there must have been some contribution from the outer parts of the desorption spot. In the simple model that led to Equation (4), only those trajectories that led in a straight line from the surface to the detection region were considered. In reality, water molecules desorbing from ASW have a wide range of take-off angles, and collisions between desorbing molecules are possible. Such collisions would broaden the TOF spectrum. In addition, the photodesorption event was not merely a statistical process that would necessarily follow Maxwell-Boltzmann statistics. However, Maxwell-Boltzmann distributions are often

useful in empirical fitting to elucidate the various dissociation or desorption channels that contribute to the total observed yield.[18]

In this case, a single desorption channel was indicated even though the TOF spectrum was slightly broader than a Maxwell-Boltzmann distribution. Therefore, the peak of the TOF spectrum was fit using Equation (3). TOF data were collected at multiple values of *r* and plotted in velocity space using the Jacobian transform, $P_v(v) = tr^2 S(t)$, where $v = r/t$ and $S(t)$ is the measured signal intensity at each time.

2.2.3. Simulation of 2 + 1 REMPI Spectra

The 2 + 1 REMPI spectrum of H_2O was simulated with PGOPHER, a freely available program for simulating rotational spectra.[20] Rotational constants of the ground and C states were taken from Yang and Skinner,[21] who used their own velocity map imaging REMPI data as well as experimental data available from the JPL spectral line catalog[22] to modify constants from Johns.[23] The nuclear spin temperature was set to 300 K, which gives an ortho:para ratio of 3:1, the statistical distribution expected at temperatures above 65 K.[24]

2.2.4. Theoretical Calculations

Ab initio methods provide a powerful means of elucidating a mechanism for the photodesorption of a water molecule from the surface of ice. Vertical singlet excitation energies of the first five singlet states of a series of small model ice clusters were benchmarked at several levels of theory, using Q-Chem 4.0 unless otherwise noted.[25] The long-range corrected (LRC) ωB97 functional in the aug-cc-pVDZ basis was found to

produce vertical excitation energies that compared well to the high-level equation-of-motion coupled-cluster singles and doubles (EOM-CCSD) method.[26, 27] The configuration interaction singles (CIS) method in the aug-cc-pVDZ basis consistently overestimated the vertical excitation energies by around 1 eV.[28, 29] However, CIS/aug-cc-pVDZ largely produced the correct ordering of the excited states of these model clusters, thus providing a correct qualitative description of the excited states. Electron attachment/detachment densities of the excited ice clusters and O-H stretching potential energy curves were obtained using CIS and ωB97 and the aug-cc-pVDZ basis. After benchmarking clusters with up to five water molecules, the effect of the bulk ice was explored using mixed quantum mechanics / molecular mechanics (QM/MM) methods.

2.3.1. EXPERIMENTAL RESULTS

The 2 + 1 REMPI spectrum of desorbed water exhibited rotational excitation, with a rotational temperature of 425 ± 75 K. In Figure 2, the peak positions and relative intensities in the REMPI spectrum of desorbed H_2O nearly match a simulated spectrum using a rotational temperature of 425 K. The experimental peaks are slightly broader than the calculated peaks, most likely due to power broadening. The fitting parameters were not guaranteed to be accurate for rotational temperatures above 300 K due to the large number of transitions and overlapping peaks. This uncertainty at high rotational temperatures may contribute to the fact that simulated spectra over quite a large range (350-500 K) fit the data, which have a considerable amount of noise due to fluctuations in both desorption and ionization laser powers. For the same experimental conditions, the

rotational temperature reported by Hama et al.[19] was 350 ± 150 K, so the results are consistent within error.

The shape of the TOF spectrum was found to be remarkably robust with respect to changes in coverage, desorption laser flux, ionization energy, desorption laser spot size, ice morphology (ASW vs. CI), and rotational state sampled. While the amount of detected water was affected by varying each of these parameters, the TOF spectra were all indistinguishable after multiplication by a scaling factor. The distribution calculated with Equation (3), using r = 3.1 mm and T_{trans} = 700 K, is shown to fit the peak of the TOF spectrum in Figure 3. The uncertainty in experimental signal intensity is shown with 95% confidence intervals. The distance from the sample to the detection region, r, was not easily measured. However, based on the method of laser alignment, r for this experiment was determined to be 3.1 ± 0.5 mm, which corresponds to T_{trans} = 700 ± 200 K (0.12 ± 0.03 eV), as both r and T_{trans} primarily affect the simulated distribution by shifting it horizontally. As mentioned in the introduction, Hama et al.[19] reported T_{trans} = 1800 ± 500 K for the same experimental conditions. Their experimental data was very similar to the data shown in Figure 3, except for a horizontal shift because their value of r was 2 mm. However, because their data was fit using the method examined in Figure 1 (with R_{max} = 6 mm), the reported translational temperature of 1800 K may be an overestimate.

Data were collected at multiple values of r. As expected, the TOF spectra shifted to lower time and narrowed as r decreased. The velocity distribution, shown in Figure 4, was consistent between data sets. Although the precise values of r shown in Figure 4 were chosen to show the best possible overlap between data sets, the distances and

uncertainties obtained by careful laser alignment were really 2.0 ± 0.5 mm, 2.5 ± 0.5 mm, and 3.1 ± 0.5 mm. Maximum signal corresponded to a velocity of ~950 m/s.

Desorption signal was found to be linear with respect to desorption laser flux. Figure 5 shows integrated water signal from 2.3 to 3.9 μs as a function of energy per pulse with r = 3.1 mm. The two different data sets were obtained with slightly different ionization energies, but both clearly show a linear dependence of signal on energy, so a single-photon mechanism of desorption is indicated.

Signal per pulse, measured at the TOF spectrum peak, was not found to require an incubation period. Within the first 32 desorption laser pulses, water signal was already maximized. Due to fluctuations in laser powers, at least 32 shots had to be averaged to obtain reproducible results. Signal also remained approximately constant after long irradiation times for initial coverages ≥ 100 L.

Water removal cross sections were measured at 1, 5, 10, 20 and 30 L exposures. With r = 2 mm, water signals at 1.1 and 2.3 μs delays were averaged over 64, 128, or 256 laser pulses by an oscilloscope, and data was collected for a total of ~100,000 pulses. These delay times were chosen to probe the faster and slower parts of the TOF spectrum. However, no significant differences in cross section were found between the cross sections at 1.1 and 2.3 μs. This result supports the idea that a single mechanism is responsible for H_2O photodesorption. Figure 6 shows two examples of the cross section measurement. The slowly decreasing water signals were fit with exponentials of the form $y = Ae^{-\sigma x}$, where x is the number of photons per cm^2 and σ is the cross section.

Although only specific rovibrational states of photodesorbed water were detected, the observed decrease in signal was caused by surface water depletion in all forms:

photodesorption of H_2O (v=0), photodesorption of H_2O (v*), and photodissociation. Multiplying all water signals by a constant did not affect the calculated cross sections; only the relative decrease in signal over irradiation time was important. Assuming that measured signal was proportional to the number of water molecules at the surface, the reported cross sections were characteristic of water removal as a whole.

Four to six cross section measurements were performed at each exposure, and the results are summarized in Figure 7. For 20-30 L, the average cross section was $(6.9 \pm 1.8) \times 10^{-20}$ cm^2. Although no statistically significant differences were found between cross sections at different exposures, 1 L exposure tended to result in lower cross sections, while 5 L exposure tended to result in higher cross sections. These trends are expected based on how water sticks to surfaces in clusters at low exposures, with maximum surface roughness around 5 L. When an attempt was made to determine the cross section at 100 L, water signal did not decrease during irradiation with 2×10^{18} photons cm^{-2}.

The TOF spectra of OH^+ and H^+ fragment ions from vibrationally excited water molecules are shown in Figure 8. The translational temperatures associated with the best fitting Maxwell-Boltzmann distributions were found to be 1400 ± 450 K for OH^+ and 1200 ± 400 K for H^+, though these temperatures should be identical according to the theory in Section 2.1. The H^+ peak was obscured by ringing from the excimer laser for the first 1 μs, so those early data points are omitted for H^+. Another complication with detecting H^+ fragments was the large H^+ signal due only to the ionization laser. Although the two H^+ peaks were slightly separated in time, some overlap did occur. Thus, only the OH^+ TOF spectrum was used to determine the parent molecule energies. The distance between the surface and the detection region was 3.0 ± 0.5 mm, and this uncertainty in

distance led to uncertainty in the translational energies of vibrationally excited parent water molecules. Based on the OH^+ data, the parent water molecules have translational energies centered around 0.24 ± 0.08 eV. Therefore, the translational energy of H_2O (v^*) is greater than that of H_2O ($v = 0$) when desorbed from ASW at 108 K by 157-nm irradiation.

The effect of increasing the irradiation fluence on the vibrationally excited water yield was determined by measuring OH^+ signal at flight times of 0.9 μs and 3.4 μs. For the desorption energies (50-90 μJ cm^{-2} per pulse) and ionization energies (4.5-5.0 mJ per pulse) used here, there was no difference other than scale between signal at the two flight times, so a single Maxwell-Boltzmann distribution was used to fit the data. Both appeared promptly, rose slowly at a linear rate, and increased by about 18% in the first ten minutes of irradiation. In a nearly identical experiment, Andersson et al.[17] found that the fast and slow signals behaved differently with increasing irradiation, so they reported a fast component with T_{trans} = 10,000 ± 2000 K and a slow component at 1800 ± 300 K. While our results match their slow component (within error), we did not detect a fast component. However, our results do not exclude the possibility of two convoluted components with similar translational temperatures. The addition of one component that does not depend on irradiation time and another that increases with irradiation time could lead to the observed signal.

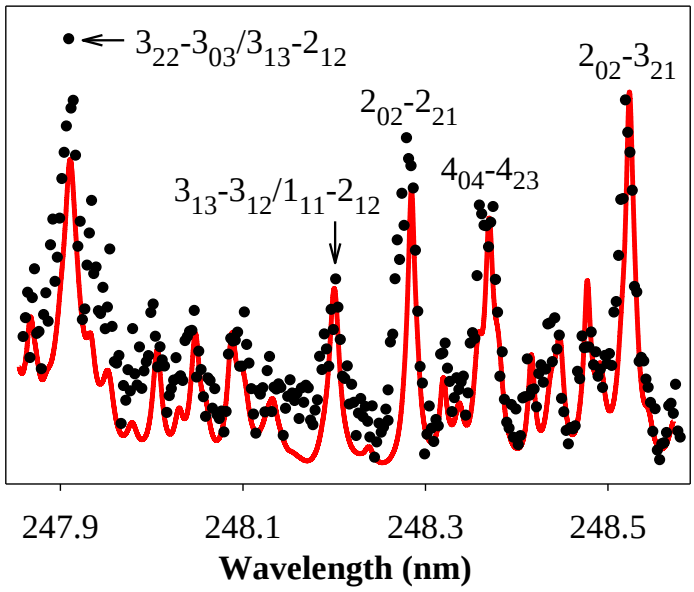

Figure 2 Experimental (2+1) REMPI spectrum of H_2O desorbed from ASW by 157-nm photons at 108 K, measured at r = 3.1 mm and t = 2.8 μs (dots), and simulated two-photon C-X spectrum with a rotational temperature of 425 K and an ortho:para ratio of 3:1 (line). The rovibrational transitions associated with the five largest peaks are shown.

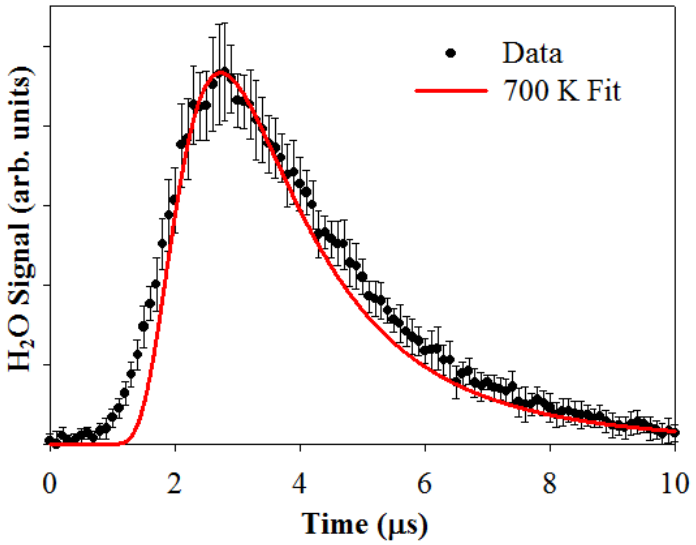

Figure 3 TOF spectrum of H_2O desorbed from ASW at 108 K by 157-nm photons and detected by (2+1) REMPI on the 2_{02}-3_{21} rotational peak at 248.52 nm. The solid line is a Maxwell-Boltzmann distribution with r = 3.1 mm and T_{trans} = 700 K.

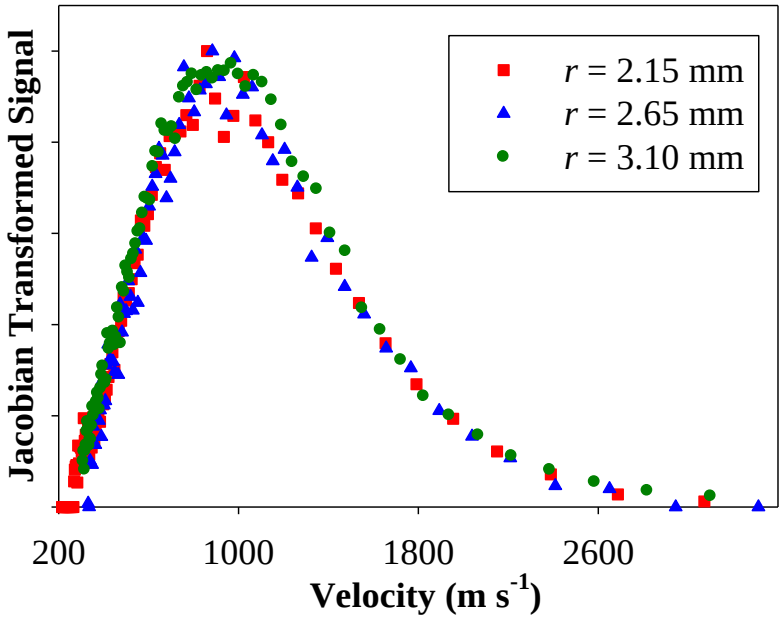

Figure 4 Velocity distribution of H_2O desorbed from ASW at 108 K by 157-nm photons and detected by (2+1) REMPI on the 2_{02}-3_{21} rotational peak at 248.52 nm. Three different distances between sample and detection region yielded consistent results.

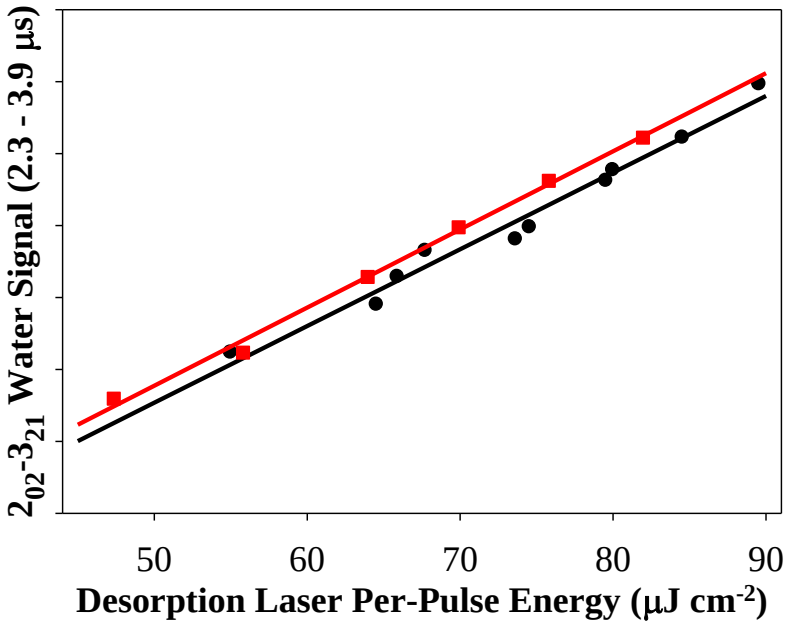

Figure 5 Water signal detected by (2+1) REMPI on the 2_{02}-3_{21} rotational peak integrated from 2.3 to 3.9 μs delay time as a function of energy per pulse. The two sets of data were obtained with slightly different ionization energies. The solid lines are linear regressions.

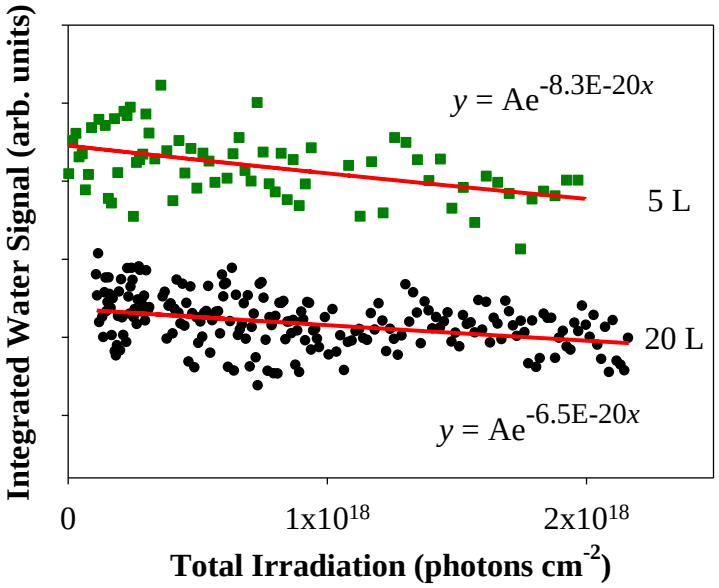

Figure 6 Representative cross section measurements for H_2O removal from 5 and 20 L ASW by 157-nm irradiation. 5 L data and exponential fitting curve were offset for clarity. The number of 157-nm photons was calculated using the pulse count on the excimer laser display and an average energy of 55 μJ cm^{-2} per pulse.

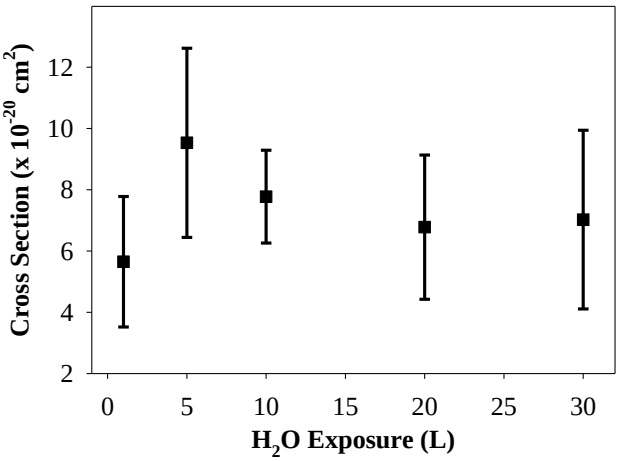

Figure 7 Average cross sections for H_2O removal from 1-30 L ASW by 157-nm irradiation. Error bars represent 95% confidence intervals based on 4-6 different measurements at each exposure.

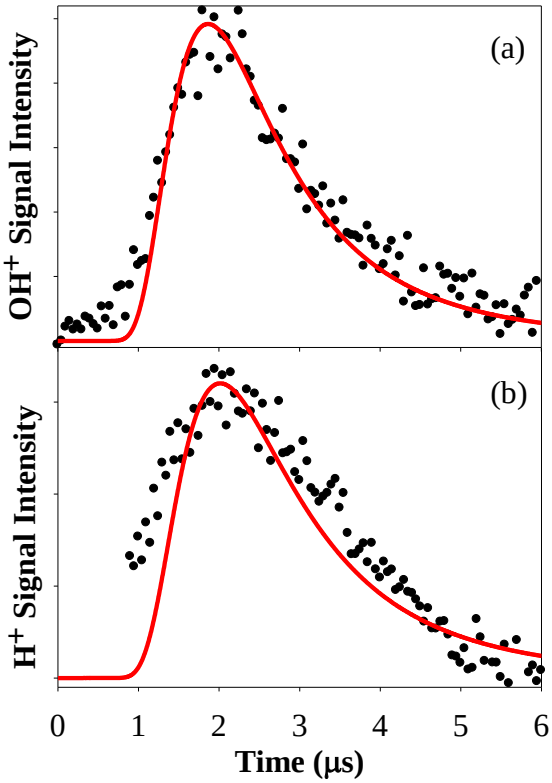

Figure 8 TOF spectra of (a) OH^+ and (b) H^+ fragment ions from vibrationally excited H_2O molecules desorbed by 157-nm photons, ionized and fragmented by 253-nm photons. A Maxwell-Boltzmann distribution with T_{trans} = 1400 K fits the OH^+ data, and a distribution with T_{trans} = 1200 K fits the peak of the H^+ spectrum.

2.4. THEORETICAL RESULTS

Figure 9 shows the calculated attachment/detachment densities of the tetramer model cluster from two different perspectives. This tetramer was extracted from a model of hexagonal ice, with the central water corresponding to one of the water molecules on the surface. This surface water molecule receives two hydrogen bonds and donates one. The attachment/detachment densities of the third singlet state of the tetramer indicate a strong dipole reversal of the surface water. As in the first singlet state (S_1) of the gas-phase

water monomer, most of the electron detachment comes from the p-orbital of the surface water oxygen, although the oxygen p-orbitals of surrounding waters also contribute. However, unlike in the water monomer, the attachment density is placed outside of the hydrogen pointing away from the surface and has mostly $4a_1$ character. This dipole reversal results in unfavorable electrostatic interactions between the surface water and its neighbors, specifically between the central oxygen and its former hydrogen-bonding partners. While the central oxygen is not quite electropositive, its atomic charge is close to zero. Thus, the excited state charge distribution seems to create an unfavorable interaction that could lead to ejection of the surface water.

Since a tetramer is still a small model system and does not incorporate contributions from the bulk of the ice, a mixed quantum mechanics/molecular mechanics (QM/MM) model system was developed. The previous tetramer model was used as the quantum mechanical region of the QM/MM system. This tetramer was surrounded by 428 water molecules in a hexagonal ice arrangement. These bulk waters were represented by an Amber TIP3P potential.[30] Interestingly, the ordering of the singlet excited states shifted when the tetramer was placed in the MM potential field. The dipole-reversal state became the first excited singlet state in the QM/MM system. To test the hypothesis that the surface water molecule would be ejected, *ab initio* molecular dynamics (AIMD) was used. In the AIMD simulations, the quantum region was modeled using CIS and the aug-cc-pVDZ basis. Simulations used randomized initial velocities consistent with a temperature of 100 K to match the experiments. Trajectories of 500 fs were computed using time steps of 0.602 fs. Due to the large number of time steps per trajectory, even the relatively modest treatment of electronic structure led to long computation times.

Hence, only a few dozen exploratory trajectories could be performed. After excitation of the cluster to the S_1 state, most trajectories showed a desorption event. However, all desorption events occurred after an abnormally long OH stretch (2.5 Å) on the ejected water. The CIS method is not necessarily reliable for such long stretches. For this reason and due to the small number of trajectories, the AIMD simulations are not sufficient to estimate the relative probabilities of dissociated versus intact products.

To further investigate the plausibility of desorption from this dipole-reversal state, excited state potential energy curves of the rigid O-H stretching of the surface quantum water in the QM/MM model were constructed at various levels of theory. Curves using the fairly robust EOM-CCSD/aug-cc-pVDZ level of theory for the QM region, displayed in Figure 10, show a barrier to O-H dissociation in the state of interest (S_1) centered around an O-H distance of 1.2 Å. This 0.54-eV barrier allows desorption to compete with the typically dominant dissociation process.

To estimate an upper-bound for the velocity of a desorbing water molecule, force and energy plots were constructed for the S_1 excited state at the CIS/aug-cc-pVDZ level of theory. The central water was pulled rigidly away from the surface, and the force on each atom was calculated at 0.1-Å intervals. The force on the central water's center of mass is plotted versus distance from the surface in Figure 11. The force plot was integrated to obtain a potential of 0.202 eV, which can be interpreted as an upper bound to the energy of a desorbing water molecule. The corresponding potential curve is shown in the inset to Figure 11. Alternatively, we also computed the difference in energies between the excited cluster at equilibrium and the excited cluster with the central water 100 Å from the surface, with a result of 0.144 eV. This value can also be considered an

upper bound to the energy of a desorbing water molecule. However, the true upper bound could be higher in energy due to the limitations of the CIS/aug-cc-pVDZ level of theory.

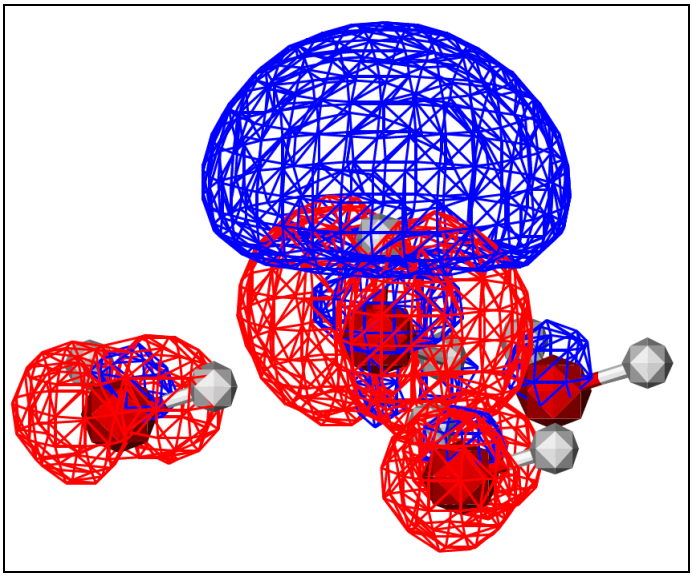

Figure 9 Electron attachment/detachment densities of the third excited singlet state of the model tetramer and the first excited state of the tetramer in the QM/MM model system(ωB97/aug-cc-pVDZ). Blue represents electron attachment density, while red represents a region of depleted electron density.

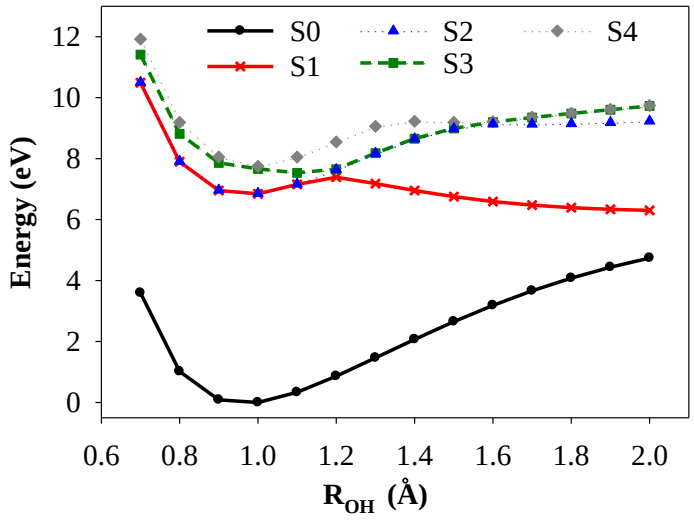

Figure 10 Ground-state (S_0) and excited state (S_1-S_4) potential energy curves of rigid OH stretching of a surface water molecule in our QM/MM model of hexagonal ice, calculated using EOM-CCSD/aug-cc-pVDZ for the quantum region and the TIP3P for the surrounding water molecules.

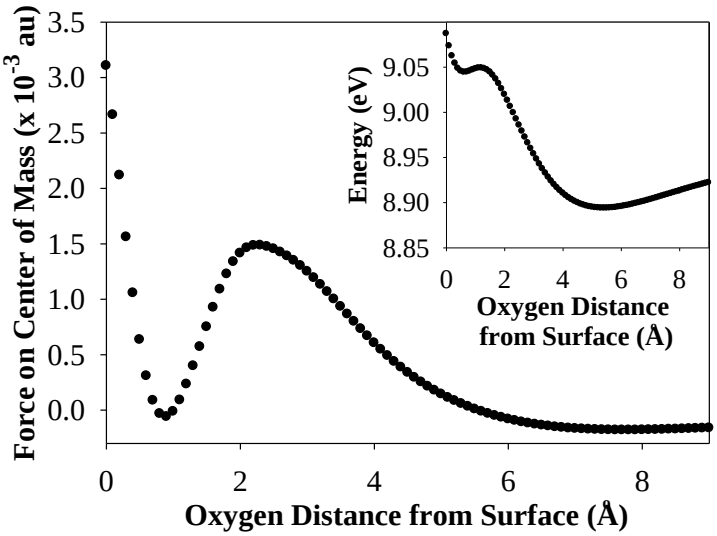

Figure 11 Force and energy (inset) plots constructed for the S_1 potential of the QM/MM model at the CIS/aug-cc-pVDZ level of theory. The central water of the quantum mechanical tetramer was pulled rigidly away from the surface.

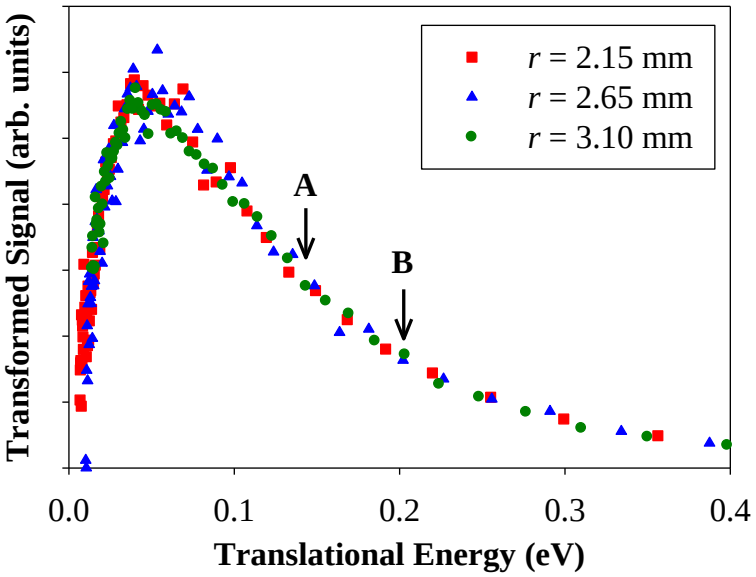

Figure 12 Translational energy distribution of H_2O desorbed from ASW at 108 K by 157-nm photons and detected by (2+1) REMPI at three different distances between the sample and the detection region. Upper bounds estimated at the CIS/aug-cc-pVDZ level of theory are shown at A (0.144 eV) and B (0.202 eV).

2.5 DISCUSSION

2.5.1. H_2O Photodesorption Mechanisms

There are several possible mechanisms for H_2O desorption following 157-nm irradiation of ASW. These mechanisms include recombinative desorption of photoproducts from different water molecules, geminate recombinative desorption of photoproducts from the same water molecule, the dipole-reversal mechanism involving a delocalized exciton, and the kick-out mechanism involving an energetic hydrogen atom. Because the TOF

spectrum in Figure 3 only requires one Maxwell-Boltzmann distribution for a good fit, one mechanism is likely responsible for the observed H_2O (v=0) signal.

Andersson et al.[17] used molecular dynamics simulations, in which only the excited water molecule was not rigid, to calculate T_{trans} = 1450 ± 150 K for the kick-out mechanism and T_{trans} = 2000 ± 200 K for geminate recombinative desorption. The products of geminate recombinative desorption exhibited significant vibrational excitation as well, but the kicked out molecules were not allowed to vibrate in these simulations. As shown in Figure 3, T_{trans} for H_2O (v=0) is only 700 ± 200 K, so neither mechanism is supported by this data. Like geminate recombination, recombination of photoproducts from different water molecules is expected to produce mostly vibrationally excited water. In addition, signal from this recombination mechanism should initially increase with irradiation time, so it is not responsible for the H_2O (v=0) signal, which only decreases in intensity with irradiation time. The only other mechanism from the list of possibilities is dipole reversal, which has not received much theoretical treatment previously.

The potential energy curves of the first excited state in Figure 10 may indicate that the charge redistribution associated with the dipole reversal leads to a quasi-bound state that allows desorption to compete with dissociation. Our results can neither confirm nor refute this mechanism, but the primary forces involved in the photodesorption event arise from charge redistribution associated with electron density depletion from the oxygen p-orbital of the surface water. Figure 11 desorption curves show that first excited state should lead to desorption, although a local minimum in the force curve indicates that the desorbing molecule may be slowed by interactions with the bulk. The estimated

upper bounds obtained from those curves are shown in Figure 12, which contains the experimental data from Figure 4 plotted as a function of translational energy. Most of the experimentally observed desorbing water has less translational energy than both computed upper bounds, which are indicated in Figure 12 by arrows at 0.144 eV (A) and 0.202 eV (B).

Photodesorption of H_2O (v*) may also be due in part to the dipole-reversal mechanism. Although the translational energy of H_2O (v*) is approximately twice that of H_2O (v=0), the same mechanism could be responsible for both. Unlike in unimolecular decay, energy conservation in the condensed phase involves neighboring molecules. After excitation, water molecules with relatively long lifetimes on the surface can lose both vibrational and translational energy to surrounding molecules, while those that desorb more quickly can retain both forms of energy. Indeed, water molecules that desorb as a result of an exciton-mediated process are expected to exhibit vibrational excitation.[19]

As mentioned in Section 3, there may be more than one mechanism responsible for desorbing H_2O (v*). Since T_{trans} for H_2O (v*) is 1400 ± 450 K, the kick-out mechanism (calculated T_{trans} = 1450 K for rigid H_2O) might be responsible for desorption of vibrationally excited water. Unfortunately, because the kicked out water molecules in the simulations of Andersson et al.[17] were not allowed to vibrate, the translational temperature of H_2O (v*) desorbing due to the kick-out mechanism has not been specifically calculated. Still, the kick-out mechanism cannot be ruled out as a mechanism for producing H_2O (v*).

Recombinative desorption of photofragments from different water molecules may also be responsible for desorption of vibrationally exited H_2O. A mechanism involving

the build-up of hydroxyl groups on the surface would help to explain why signal indicative of H_2O (v*) increases with irradiation time. As photodissociation occurs, more OH radicals become available for recombination: OH + OH → H_2O + O. The irradiation time dependence results can be explained if both recombinative desorption and one of the direct mechanisms of desorption lead to translational temperatures near 1400 K.

2.5.2. Photodesorption Cross Section

In the present cross section experiments, only H_2O (v=0) molecules are detected, but the calculated cross sections are characteristic of total water removal from the ice surface. With increasing irradiation, H_2O (v=0) signal declines due to the decreasing number of surface water molecules, which are removed through both photodesorption and photodissociation. According to Oberg et al.,[6] at 100 K, 64% of water loss is attributed to intact desorption, while the rest is attributed to dissociation. The average cross section we measured for 20-30 L exposure was $(6.9 \pm 1.8) \times 10^{-20}$ cm^2. Assuming that 64% of water loss is due to desorption, the cross section of intact H_2O desorption would be approximately $(4.4 \pm 1.2) \times 10^{-20}$ cm^2. However, Oberg et al.[6] used a hydrogen discharge lamp with up to 10.5-eV photons, so it is probable that an even greater ratio of desorption relative to dissociation occurs with only 7.9-eV photons. A more extensive discussion of the wavelength dependence follows later in this section.

The lowest cross section observed in these experiments, 5.7×10^{-20} cm^2 for 1 L exposure, is slightly higher than the 2.3×10^{-20} cm^2 cross section reported from 6.4-eV irradiation of 0.6 ML H_2O on p(2x2)O/Pd(111).[31] Higher coverage and photon energy are responsible for making our cross sections higher.

The water desorption cross section that most astrophysical models utilize, 8 x 10^{-18} cm^2, was determined for Lyman-α photons (10.2 eV) using a microbalance to measure total ice removal from the surface.[7] This value is two orders of magnitude larger than the cross section obtained in the present experiments. Quadrupole detection of D_2 from D_2O ice at 126 nm led to an estimate of 9 x 10^{-18} cm^2 for the cross section of ice destruction, which includes desorption, dissociation, and ionization.[32] Because it includes ionization, the ice destruction cross section should be much larger than the water removal cross section. Therefore, the water removal cross section at 10.2 eV may actually be much lower than the estimate of Westley et al.[7] Even if the true value is significantly lower than 8 x 10^{-18} cm^2, the water removal cross section at 7.9 eV (6.9 x 10^{-20} cm^2) will likely provide a lower limit.

The most important difference between these two experiments is the wavelength of photons used. The absorption coefficient at 10.2 eV is approximately twice the value at 7.9 eV for amorphous ice.[5] If the same mechanisms were dominant at 10.2 eV and 7.9 eV, the cross section would only be expected to be twice as large at 10.2 eV. However, additional mechanisms of ice removal could be responsible for making the cross section at 10.2 eV so large. The photoelectric threshold of ASW is 8.7 eV, and the photoelectric yield at 10 eV is ~ 10^{-3} per photon.[33] Therefore, photoionization of water plays a significant role in ice removal at 10.2 eV, while it is negligible at 7.9 eV. Once H_2O^+ is formed, it can react and recombine with electrons to form an excited state similar to the dipole reversal state described in this paper. This excited state could lead to desorption or decay to form other species.[34] Figure 10 shows deeper bound states for higher energy excited states that can be accessed with 10.2-eV photons. These have longer lifetimes,

and, since desorption yields scale as $Y \sim \exp(-\tau_c \Gamma)$, where Γ is the bandwidth and τ_c is the critical excited state lifetime,[35] they should also have higher desorption yields.

An extensive study of the H_2O photodesorption yield using a hydrogen discharge lamp (7-10.5 eV) obtained a yield of 4.5×10^{-3} molecules photon^{-1} for exposures greater than 8 L at 100 K,[6] which is close to the corresponding yield from Westley et al. of 7.5×10^{-3} molecules photon^{-1}.[7] These similar results led Oberg et al. to hypothesize that the photodesorption yield would not be affected by different lamp spectral energy distributions.[6] While all hydrogen discharge lamps may give similar yields due to their common high-energy photons, the wavelength of the irradiation source does make an enormous difference. The yield has not been determined from the present experiments because the relationship between water signal and thickness is unknown. However, for 1 L exposure, as stated above, clusters are likely to form. Under these conditions, the maximum coverage is assumed to be 10^{14} molecules. Assuming that signal is proportional to coverage, an estimate of the yield is 1.8×10^{-4} molecules photon^{-1}. Therefore, our estimated yield is about one order of magnitude below the corresponding yield from Oberg et al., 1.3×10^{-3} molecules photon^{-1}.[6]

2.5.3. Astrophysical Implications

Clearly, cross section and yield are greatly influenced by the UV wavelength and flux. The interstellar UV field is often simulated with a hydrogen discharge lamp since the Lyman-α flux is dominant. However, many regions within our solar system are not dominated by the Lyman-α flux. Calculations intended to model a specific location in space should obviously use the cross sections specific to the prevailing UV wavelengths

in the area. In addition, though not explicitly shown in this study, the ice surface temperature can play a large role in determining cross sections for dissociation and desorption, mainly due to increases in excited state lifetimes as increasing temperature reduces coupling between neighbors.[36, 37]

As an example, the cross sections presented in this paper apply to the rings of Saturn, which are comprised of icy grains with temperatures near 100 K. The solar photon flux below 230 nm near Saturn is 3.5×10^{11} photons cm^{-2} s^{-1}.[38] In the previous section, we stated that the cross section of intact H_2O desorption would be approximately 4.4×10^{-20} cm^2, assuming that 64% of our measured cross section is due to intact desorption and that the remainder is due to dissociation. We can then calculate a rate of desorption by multiplying the photon flux by the cross section and the number of molecules on the surface of a grain. For a grain with a radius of 1 cm, the result is 4.8×10^7 molecules s^{-1}. Using the value from Westley et al.[7] would instead give a rate of 8.8×10^9 molecules s^{-1}, but this rate would include dissociation and ionization in addition to intact desorption. Since the solar photon flux below 230 nm includes more photons above 7.9 eV than below, our calculated rate of 4.8×10^7 molecules s^{-1} for intact H_2O desorption from a 1-cm grain should be treated as a lower bound.

2.6. CONCLUSIONS

The photodesorption of water molecules from amorphous solid water by 157-nm irradiation has been examined using resonance-enhanced multiphoton ionization. The rotational temperature has been determined, by comparison with simulations, to be 425 ± 75 K. The time-of-flight (TOF) spectrum of H_2O ($v = 0$) has been fit with a Maxwell-

Boltzmann distribution with a translational temperatures of 700 ± 200 K (0.12 ± 0.03 eV). H^+ and OH^+ fragment ions have been detected with non-resonant multiphoton ionization, indicating vibrationally excited parent water molecules with translational energies of 0.24 ± 0.08 eV. These results have been compared and contrasted with those of Hama et al.[19] and Andersson et al.[17] The cross section for ice removal by 7.9-eV photons near 100 K varies with coverage, averaging (6.9 ± 1.8) x 10^{-20} cm^2 for > 10 L H_2O exposure. Electronic structure computations have also probed the excited states of water and the mechanisms of desorption. Calculated electron attachment and detachment densities show that exciton delocalization leads to a dipole reversal state in the first singlet excited state of a model system of hexagonal water ice. *Ab Initio* Molecular Dynamics (AIMD) simulations show possible desorption of a photo-excited water molecule from this cluster, though the non-hydrogen bonded OH bond is stretched significantly before desorption. Potential energy curves of this OH stretch in the electronic excited state show a barrier to dissociation, lending credence to the dipole reversal mechanism.

Chapter 3

Raman Spectra of DNA Nucleobases

3.1. INTRODUCTION

Many studies have shown that low-energy electrons (LEEs) can cause a range of events that damage DNA. [39-41] These damage events include strand breaks, nucleobase damage, or base-release through glycosidic bond cleavage. Measurement of these events is typically difficult, and relies on post-irradiation analysis techniques including high-pressure liquid chromatography, gel electrophoresis,[39-40] and fluorescence tagging. It would be highly useful to have a method to directly measure DNA damage, without relying on complicated post-irradiation analysis. Sidorov[42] has developed a method of directly probing DNA damage events utilizing the interactions of DNA with monolayer graphene on nanostructured gold thin films. After placing the DNA on the graphene, a broad-beam electron source was used to irradiate the sample. Prior to and after irradiation, Raman spectroscopy was used to characterize DNA damage.

In order to support experiment, Raman spectra were simulated of the DNA bases on a model graphene surface. In this case, the graphene surface was represented by circumcoronene. Circumcoronene, $C_{54}H_{18}$, is a polycyclic aromatic hydrocarbon. Its geometry is similar to graphene, except that there are hydrogens on the edge carbons. Thus, circumcoronene should be a reasonable model for graphene in circumstances where the adsorbing molecules do not encounter the edge hydrogens. Circumcoronene, adenine, thymine, guanine, and cytosine were each optimized at the PBE-D3/def2-SV(P) level of theory using the Turbomole quantum chemistry package. After optimization of the

monomers, constrained optimizations of the nucleobases on the circumcoronene were performed. In these optimizations, all circumcoronene nuclei were fixed. Analysis of the vibrational frequencies of the obtained structures of the monomers indicated that these were local minima structures. However, there were imaginary frequencies in the structures of the nucleobases/circumcoronene complexes, due to constraining the circumcoronene. These imaginary frequencies correspond to vibrational modes in the circumcoronene, which wasn't allowed to move in the optimization. In order to see some of the basis set effects on the Raman shift due to being on graphene, optimizations and frequency calculations were repeated at the PBE-D3/def2-TZVP level of theory.

3.2. RESULTS

The Raman spectra of the nucleobases themselves and of the spectra of the nucleobases on a graphene surface are shown in Figures 13-24. The differences in spectra between the def2-SV(P) and def2-TZVP basis sets were fairly small. The mean shifts were 6.4, 7.2, 6.8, and 6.9 cm^{-1} for adenine, cytosine, guanine, and thymine respectively. However, the relative intensities of these peaks varied with the basis set. Of more interest is the Raman shift of each nucleobase when it is placed on a graphene surface. For adenine, cytosine, guanine, and thymine, the mean shifts at def2-TZVP basis were 8.4, 8.2, 20.1, and 9.2 cm^{-1} respectively. These shifts, other than for guanine, are small.

Of more interest than the shifts themselves are the effects on the intensity of the peaks. Comparing the spectra (figures 17-24) of the isolated nucleobases to those on the graphene surface, some peaks seem to have disappeared. These peaks are still present, but other peaks have been enhanced by the surface so much that the relative intensities

have been greatly reduced. For adenine, the peaks that were especially enhanced were 871.8 cm^{-1} (a N-C-N bending) and 963.2 cm^{-1} (a hydrogen wagging). For cytosine, 1225.2 cm^{-1} (a combination of hydrogen wagging and a ring twist) and 901.4 cm^{-1}(N-C-N bending) were prominently enhanced peaks. The enhanced modes for guanine were at 801.5 cm^{-1} and 1083.2 cm^{-1}. For thymine, the peaks 874.63, 1204.9, and 1324.7 cm^{-1} are enhanced by the surface. The enhanced peaks are the peaks that should show up clearly in an experimental Raman spectrum. It would be very interesting to compare the predicted spectra to experiment in this thesis. Unfortunately, at this time the experimental work is underway, and that data is not available currently.

3.3 CONCLUSIONS

Raman spectra of isolated nucleobases and nucleobases on a graphene surface have been calculated. Raman spectra of the isolated nucleobases computed with at PBE-D3/SV(P) are a little different than those obtained with the larger TZVP basis set. The mean shifts from double-zeta to triple-zeta were 6.4, 7.2, 6.8, and 6.9 cm^{-1} for adenine, cytosine, guanine, and thymine respectively. The shifts of the Raman frequencies due to the circumcoronene surface are essentially the same with both double and triple zeta basis sets. Raman spectra of the nucleobases on circumcoronene show a massive increase in intensity in a few peaks. These predicted spectra should help experimentalists with peak identification.

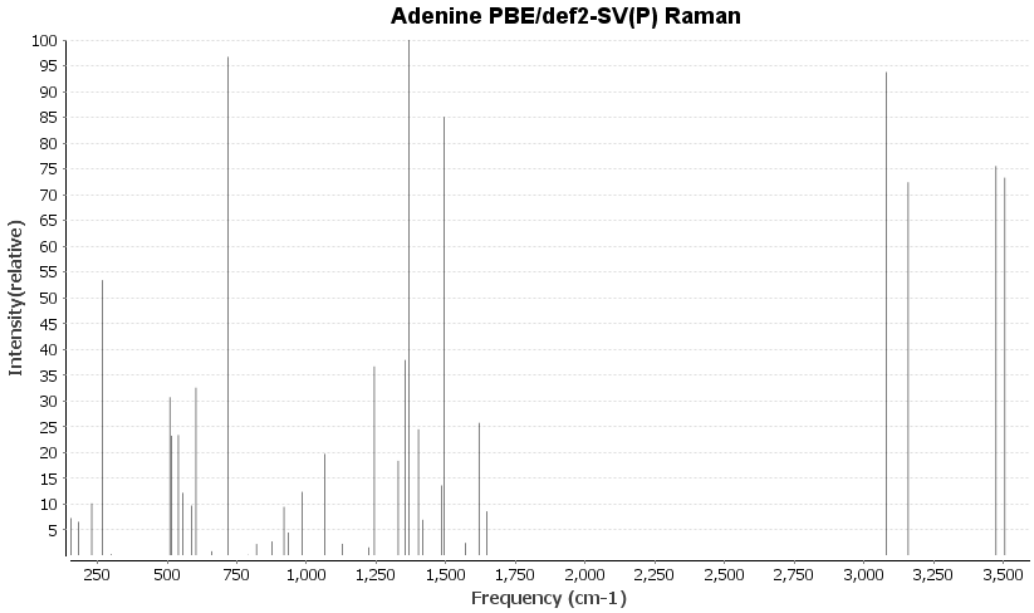

Figure 13 Raman Spectra of Adenine at PBE/def2-SV(P) level of theory.

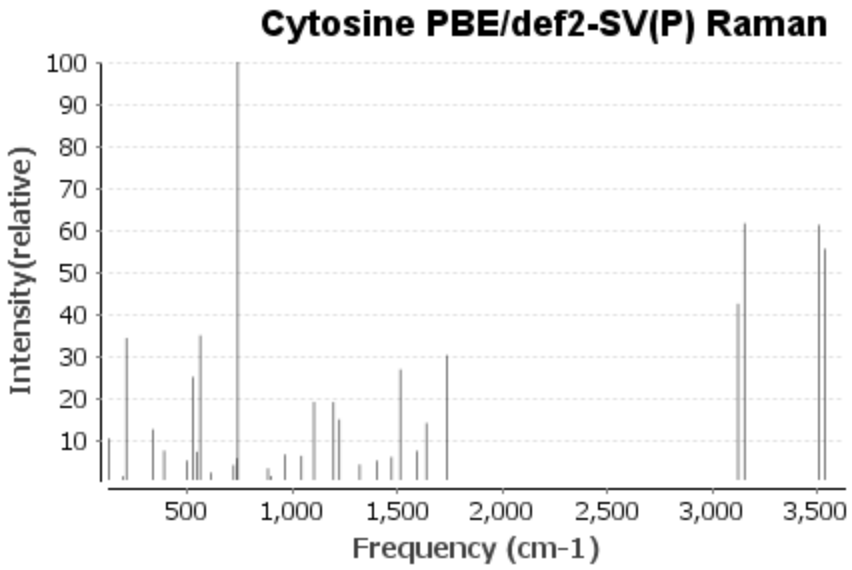

Figure 14 Raman spectra of cytosine at PBE-D3/def2-SV(P).

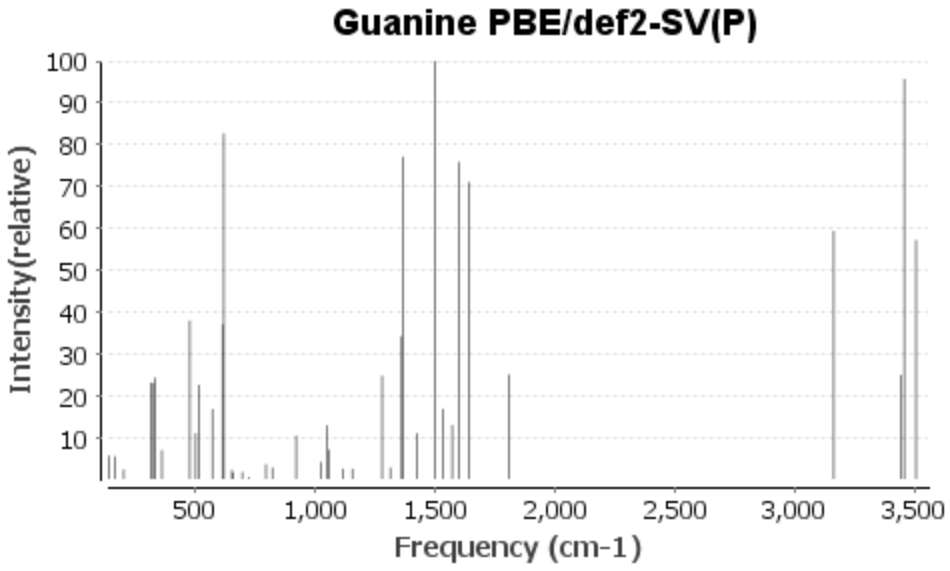

Figure 15 Raman spectra of guanine at PBE-D3/def2-SV(P).

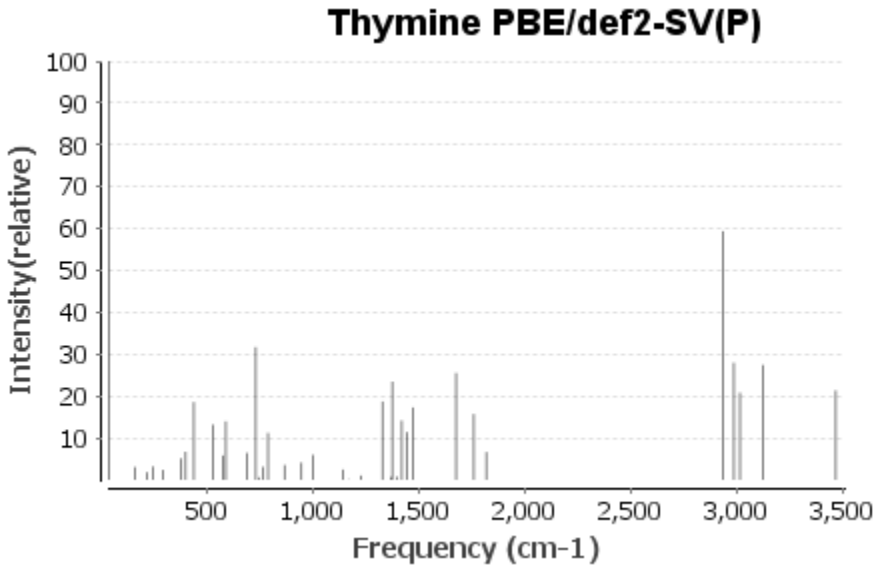

Figure 16 Raman spectra of thymine at PBE-D3/def2-SV(P).

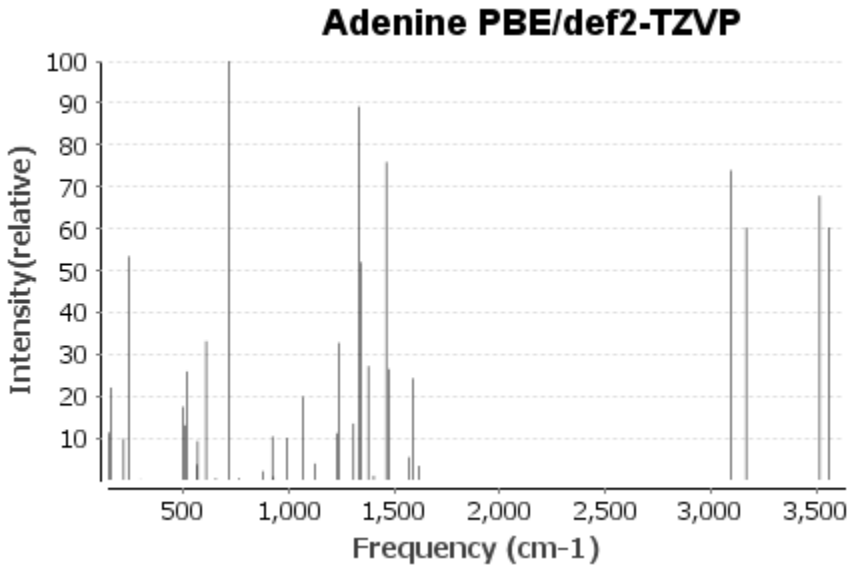

Figure 17 Raman spectra of adenine at PBE-D3/def2-TZVP.

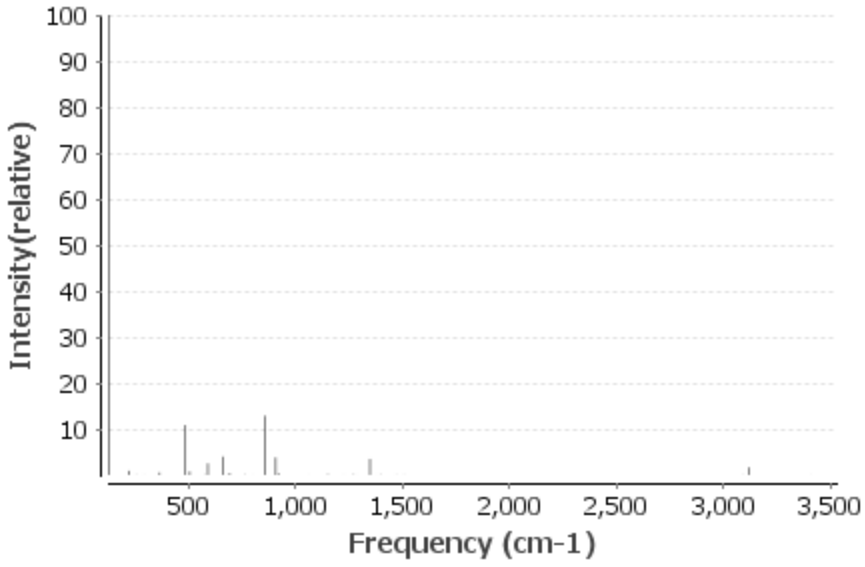

Figure 18 Raman spectra of Adenine on a circumcoronene surface at PBE-D3/def2-TZVP.

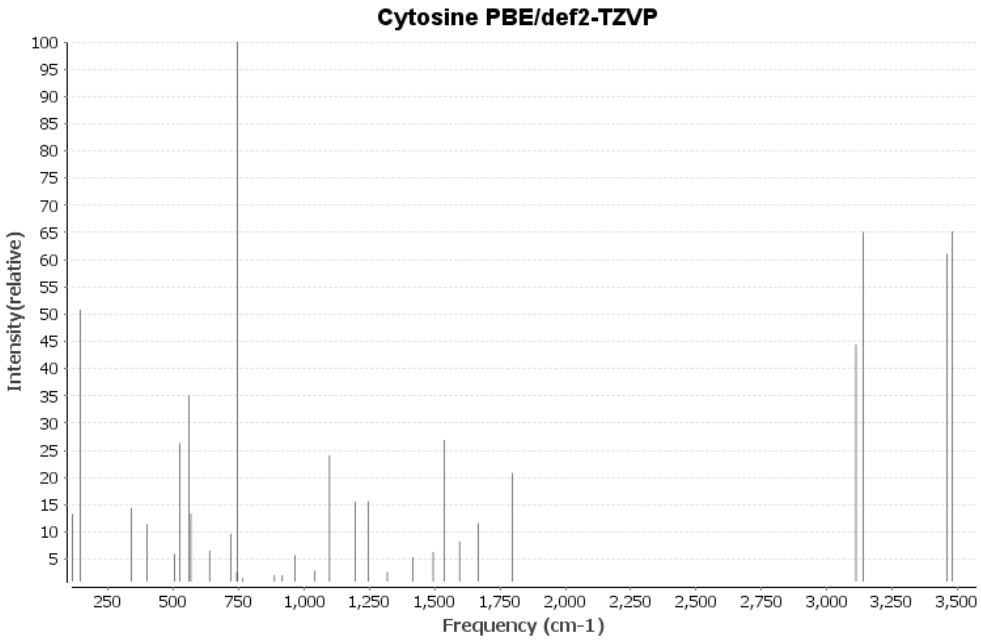

Figure 19 Raman spectra of cytosine at PBE-D3/def2-TZVP.

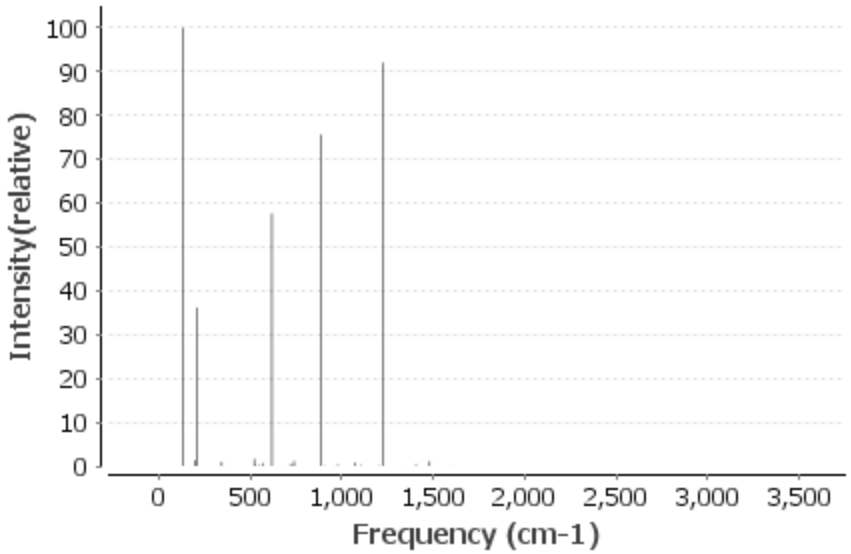

Figure 20 Raman spectra of cytosine on a circumcoronene surface at PBE-D3/def2-TZVP.

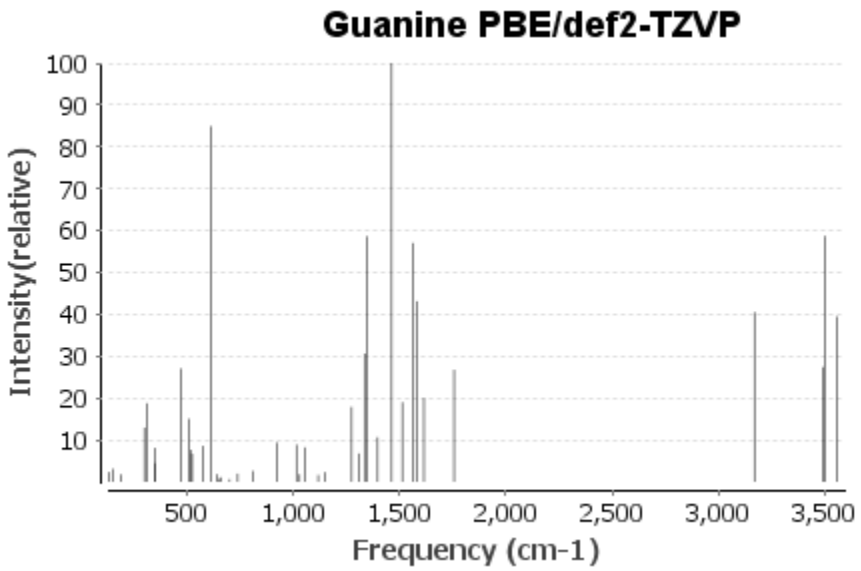

Figure 21 Raman spectra of guanine at PBE-D3/def2-TZVP.

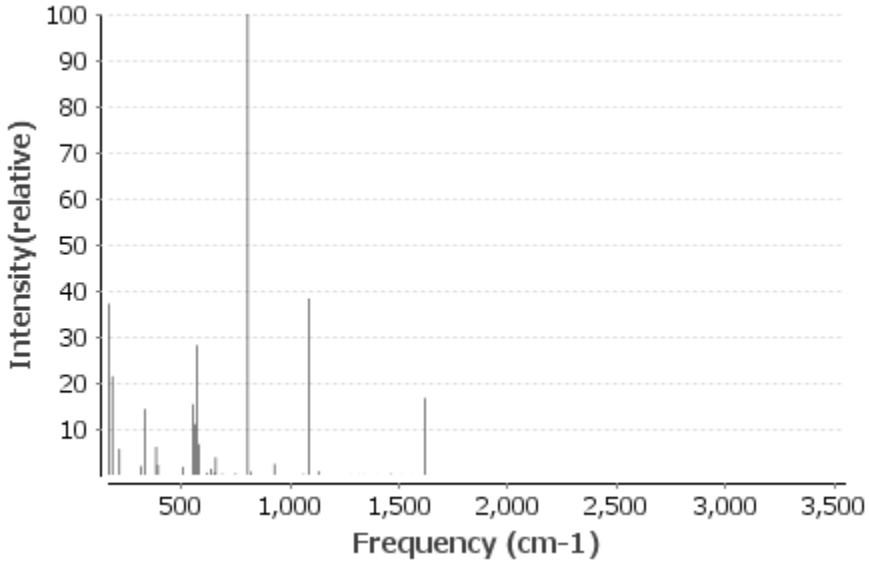

Figure 22 Raman spectra of guanine on circumcoronene at PBE-D3/def2-TZVP.

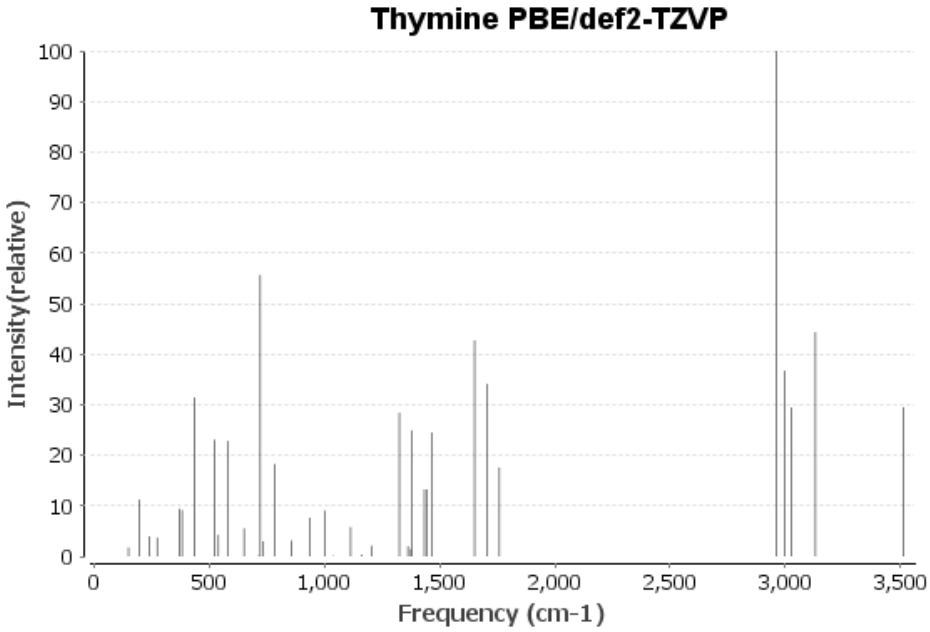

Figure 23 Raman spectra of thymine at PBE-D3/def2-TZVP.

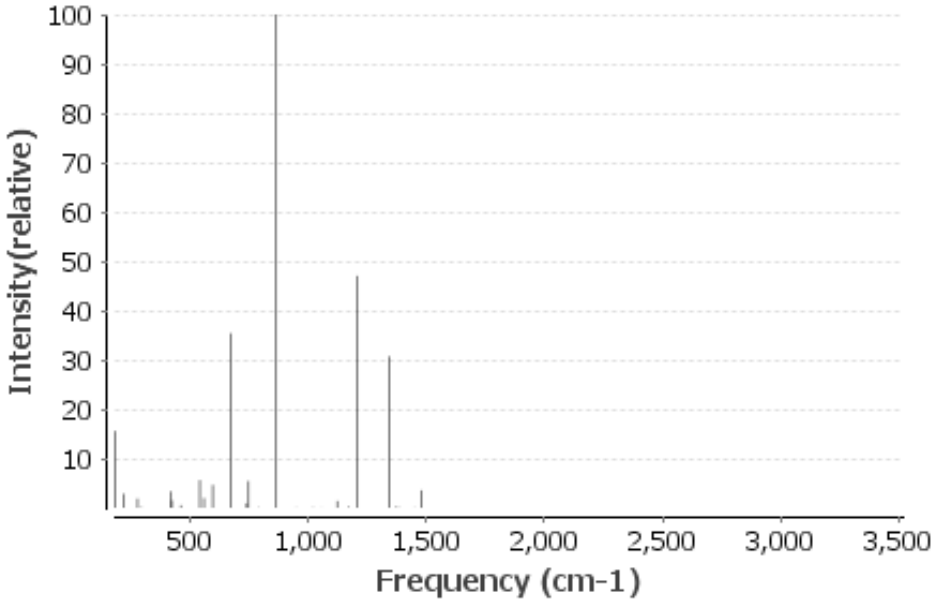

Figure 24 Raman spectra of thymine on circumcoronene at PBE-D3/def2-TZVP.

REFERENCES

1. M. E. Brown, E. L. Schaller and W. C. Fraser, Astronomical Journal **143** (6), 7 (2012).

2. S. Vahidinia, J. N. Cuzzi, M. Hedman, B. Draine, R. N. Clark, T. Roush, G. Filacchione, P. D. Nicholson, R. H. Brown, B. Buratti and C. Sotin, Icarus **218** (1), 736-736 (2012).

3. C. Dominik, C. Ceccarelli, D. Hollenbach and M. Kaufman, Astrophysical Journal **635** (1), L85-L88 (2005).

4. D. M. Chipman, Journal of Chemical Physics **124** (4), 9 (2006).

5. K. Kobayashi, Journal of Physical Chemistry **87** (21), 4317-4321 (1983).

6. K. I. Oberg, H. Linnartz, R. Visser and E. F. van Dishoeck, Astrophysical Journal **693** (2), 1209-1218 (2009).

7. M. S. Westley, R. A. Baragiola, R. E. Johnson and G. A. Baratta, Nature **373** (6513), 405-407 (1995).

8. M. Y. Kulikov, A. M. Feigin, S. K. Ignatov, P. G. Sennikov, T. Bluszcz and O. Schrems, Atmospheric Chemistry and Physics **11** (4), 1729-1734 (2011).

9. N. Nishi, H. Shinohara and T. Okuyama, Journal of Chemical Physics **80** (8), 3898-3910 (1984).

10. T. Hama, M. Yokoyama, A. Yabushita, M. Kawasaki and N. Watanabe, Nuclear Instruments & Methods in Physics Research Section B-Beam Interactions with Materials and Atoms **269** (9), 1011-1015 (2011).

11. S. Andersson and E. F. van Dishoeck, Astronomy & Astrophysics **491** (3), 907-916
(2008).

12. C. Arasa, S. Andersson, H. M. Cuppen, E. F. van Dishoeck and G. J. Kroes, Journal of Chemical Physics **132** (18), 12 (2010).

13. P. H. Hahn, W. G. Schmidt, K. Seino, M. Preuss, F. Bechstedt and J. Bernholc, Physical Review Letters **94** (3), 4 (2005).

14. A. Acocella, G. A. Jones and F. Zerbetto, J. Phys. Chem. Lett. **3**, 3610-3615 (2012).

15. A. J. DeSimone, B. O. Olanrewaju, G. A. Grieves and T. M. Orlando, Journal of Chemical Physics **138** (8) (2013).

16. N. G. Petrik and G. A. Kimmel, Journal of Physical Chemistry B **109** (33), 15835-15841 (2005).

17. S. Andersson, C. Arasa, A. Yabushita, M. Yokoyama, T. Hama, M. Kawasaki, C. M. Western and M. N. R. Ashfold, Physical Chemistry Chemical Physics **13** (35), 15810-15820 (2011).

18. F. Zimmermann and W. Ho, Surface Science Reports **22** (4-6), 127-247 (1995).

19. T. Hama, M. Yokoyama, A. Yabushita, M. Kawasaki, S. Andersson, C. M. Western, M. N. R. Ashfold, R. N. Dixon and N. Watanabe, Journal of Chemical Physics **132** (16), 8 (2010).

20. PGOPHER, a Program for Simulating Rotational Structure, C. M. Western, University of Bristol, http://pgopher.chm.bris.ac.uk.

21. M. Yang and J. L. Skinner, Physical Chemistry Chemical Physics **12** (4), 982-991 (2010).

22. H. M. Pickett, R. L. Poynter, E. A. Cohen, M. L. Delitsky, J. C. Pearson and H. S. P. Muller, Journal of Quantitative Spectroscopy & Radiative Transfer **60** (5), 883-890 (1998).

23. J. W. C. Johns, Canadian Journal of Physics **49** (7), 944-& (1971).

24. B. P. Bonev, M. J. Mumma, G. L. Villanueva, M. A. Disanti, R. S. Ellis, K. Magee-Sauer and N. Dello Russo, Astrophysical Journal **661** (1), L97-L100 (2007).

25. A. I. Krylov and P. M. W. Gill, Wiley Interdisciplinary Reviews-Computational Molecular Science **3** (3), 317-326 (2013).

26. J. D. Chai and M. Head-Gordon, Journal of Chemical Physics **128** (8), 15 (2008).

27. J. F. Stanton and R. J. Bartlett, Journal of Chemical Physics **98** (9), 7029-7039 (1993).

28. J. E. Delbene, Ditchfie.R and J. A. Pople, Journal of Chemical Physics **55** (5), 2236-& (1971).

29. J. B. Foresman, M. Headgordon, J. A. Pople and M. J. Frisch, Journal of Physical Chemistry **96** (1), 135-149 (1992).

30. W. L. Jorgensen, J. Chandrasekhar, J. D. Madura, R. W. Impey and M. L. Klein, Journal of Chemical Physics **79** (2), 926-935 (1983).

31. X. Y. Zhu, J. M. White, M. Wolf, E. Hasselbrink and G. Ertl, Journal of Physical Chemistry **95** (21), 8393-8402 (1991).

32. N. Watanabe, T. Horii and A. Kouchi, Astrophysical Journal **541** (2), 772-778 (2000).

33. B. Baron, D. Hoover and F. Williams, Journal of Chemical Physics **68** (4), 1997-1999 (1978).

34. G. A. Kimmel and T. M. Orlando, Physical Review Letters **75** (13), 2606-2609 (1995).

35. A. R. Burns, E. B. Stechel, D. R. Jennison and T. M. Orlando, Physical Review B **45** (3), 1373-1385 (1992).

36. J. Herring-Captain, G. A. Grieves, A. Alexandrov, M. T. Sieger, H. Chen and T. M. Orlando, Physical Review B **72** (3), 10 (2005).

37. M. T. Sieger, W. C. Simpson and T. M. Orlando, Physical Review B **56** (8), 4925-4937 (1997).

38. T. Encrenaz, R. Kallenbach, T. C. Owen and C. Sotin, *The Outer Planets and their Moons*. (Springer, Dordrecht, The Netherlands, 2005).

39. B. Boudaiffa, P. Cloutier, D. Hunting, M. A. Huels, L. Sanche. Resonant Formation of DNA Strand Breaks by Low-Energy (3 to 20 eV) Electrons. Science **287**, 1658−1660 (2000).

40. B. Boudaiffa, D. Hunting, P. Cloutier, M.A. Huels, L. Sanche. Introduction of Single- and Double-Strand Breaks in Plasmid DNA by 100-1500 eV Electrons. International Journal of Radiation Biology **76,** 1209-1221 (2000).

41. T.M. Orlando, D. Oh, Y. Chen, A.B. Aleksandrov. Low-Energy Electron Diffraction and Induced Damage in Hydrated DNA. Journal of Chemical Physics **128**, 195102 (2008).

42. A.N. Sidorov, T.M. Orlando. Monolayer Graphene Platform for the Study of DNA Damage by Low-Energy Electron Irradiation, Journal of Physical Chemistry Letters 4, 2328-2333 (2013).